Available online at www.sciencedirect.com
ScienceDirect
Biosensors and Bioelectronics 23 (2008) 1503–1511
BIOSENSORS & BIOELECTRONICS
www.elsevier.com/locate/bios

Non-Faradaic electrochemical detection of protein interactions by integrated neuromorphic CMOS sensors

Blake C. Jacquot [a,*], Nini Muñoz [a,1], Darren W. Branch [b], Edwin C. Kan [a]

[a] *School of Electrical and Computer Engineering, Cornell University Ithaca, 323 Phillips Hall, Ithaca, NY 14853 USA*
[b] *Biosensors and Nanomaterials Department, Sandia National Laboratories, Albuquerque, NM 87185, USA*

Received 27 October 2007; received in revised form 17 December 2007; accepted 3 January 2008
Available online 16 January 2008

Abstract

Electronic detection of the binding event between biotinylated bovine serum albumen (BSA) and streptavidin is demonstrated with the chemoreceptive neuron MOS (CνMOS) device. Differing from the ion-sensitive field-effect transistors (ISFET), CνMOS, with the potential of the extended floating gate determined by both the sensing and control gates in a neuromorphic style, can provide protein detection without requiring analyte reference electrodes. In comparison with the microelectrode arrays, measurements are gathered through purely capacitive, non-Faradaic interactions across insulating interfaces. By using a (3-glycidoxypropyl)trimethoxysilane (3-GPS) self-assembled monolayer (SAM) as a simple covalent link for attaching proteins to a silicon dioxide sensing surface, a fully integrated, electrochemical detection platform is realized for protein interactions through monotone large-signal measurements or small-signal impedance spectroscopy. Calibration curves were created to coordinate the sensor response with ellipsometric measurements taken on witness samples. By monitoring the film thickness of streptavidin capture, a sensitivity of 25 ng/cm^2 or 2 Å of film thickness was demonstrated. With an improved noise floor the sensor can detect down to 2 ng/(cm^2 mV) based on the calibration curve. AC measurements are shown to significantly reduce long-term sensor drift. Finally, a noise analysis of electrochemical data indicates $1/f^{\alpha}$ behavior with a noise floor beginning at approximately 1 Hz.

Keywords: Biosensor; MOSFET; FET; Protein microarray

1. Introduction

Integrated electrochemical sensors for biological detection hold promise as a prompt, inexpensive method for initial on-site diagnosis (Drummond et al., 2003; Bakker, 2004), and can complement more costly and bulky in-lab optical methods (Thevenot et al., 2001; Wilson et al., 2001). The use of complementary metal-oxide-silicon (CMOS) integrated circuits (IC) enables small, tightly controlled sensors that can be distributed widely. Principal concerns for field-deployable sensors include reliability, predictable signal drift, and, for extended use, low-power consumption. Long-term reliability results primarily from employing robust materials, such as silicon nitride and Teflon for device isolation and sensing interface coating (Cane et al., 1996). The omnipresent problem of signal drift is often addressed through reference circuitry or by post-processing the data if the drift is consistent. Low-power consumption has largely not been addressed.

Field effect transistor (FET) sensors based on CMOS have a long history of usage in electrochemical detection (Bergveld, 2003). Traditionally, the gate metal is removed and sensing is performed on the gate oxide or coatings, while a reference electrode such as Ag/AgCl or Pt in the analyte induces the field effect at the appropriate operating point. The attachment of ion-selective membranes across the gate oxide can result in specific ion sensing, commonly called the ion-sensitive field-effect transistor (ISFET). Work has predicted device sensitivity down to a single ion, such as a proton for pH detection (van Hal et al., 1996). Primarily, efforts have focused on DC measurements.

Efforts for ISFET-style devices beyond ion detection have expanded to include the interactions of proteins in an ISFET context. Various tethering schemes have been reported in an impedance spectroscopy configuration (Katz and Willner, 2003; Sadik et al., 2002). Such FET-based devices, though successful,

* Corresponding author. Tel.: +1 607 254 8842; fax: +1 607 254 3508.
E-mail addresses: bcj7@cornell.edu (B.C. Jacquot), nlm9@cornell.edu (N. Muñoz), dwbranc@sandia.gov (D.W. Branch), kan@ece.cornell.edu (E.C. Kan).
[1] Tel.: +1 607 254 8842; fax: +1 607 254 3508.

0956-5663/$ – see front matter © 2008 Elsevier B.V. All rights reserved.
doi:10.1016/j.bios.2008.01.006

diminish the full potential of CMOS integration for microarrays since the scaling advantages of CMOS are overshadowed by the need for a relatively large, highly stable reference electrode.

Microelectrode array sensors based on IC technology have also been exploited for protein or cells through large-signal AC or impedance spectroscopy measurements. Most use metals such as gold or platinum that are incompatible with CMOS processing (Radke and Alocilja, 2004; Pei et al., 2001; Saum et al., 1998; DeSilva et al., 1995). Use of aluminum pads by conventional CMOS foundry was investigated (Hassibi and Lee, 2006), where heating of the sensor interface from localized power dissipation due to charge transfer was observed. Most microelectrode arrays require some variation on potentiostats to record data. For example, the conductive microelectrodes can serve as the auxiliary and working electrodes, while a reference electrode provides the stable cell potential.

In this study, we present the first FET-based sensing by a single AC frequency to detect protein binding in real time without the use of a reference electrode or gold or platinum interfaces. Elimination of the reliance on the reference electrode is achieved by using an extended floating gate in the chemoreceptive neuron MOS (CνMOS) device (Jacquot et al., 2005, 2006; Shen et al., 2003, 2004). The output current is a function of the floating gate potential, which maintains the advantages from high transconductance in the FET. The floating gate potential is determined by both the sensing gate exposed to the analyte and an internal control gate which can serve to set the operating point and inject the AC excitation. The ability to directly detect protein binding in fluid will be evaluated. Current fabrication of the solid-state sensor uses only CMOS-compatible materials and displays very low signal drift. The results show strong potential for CνMOS as a protein sensor in microarray integration.

2. Materials and methods

2.1. Device design

The CνMOS structure reduces the invasiveness of detection while allowing full integration of sensor and supporting circuits through commercial fabrication with minimal post-processing. The inclusion of several sensing and control gates coupled to a single floating gate creates a neuron-like effect, analogous to several weighted inputs connected to a single node (Shibata and Ohmi, 1992; Minch et al., 1996). AC or DC biasing is delivered through the control gate, and, although not strictly necessary, the fluid bulk potential can be further stabilized by fringing fields or by integrated electrodes. Later work has provided additional theoretical analysis on a similar system (Barbaro et al., 2006).

The CνMOS device was fabricated through the AMIS 1.5 μm CMOS process (MOSIS). Tests presented in this paper were performed on devices containing a single sensing gate (SG) that had a native SiO_2 over the second polysilicon layer. Sensing gate dimensions ranged from 23 μm × 360 μm to 157 μm × 360 μm. The FET can be biased from the control gate (CG) independently of the sensing interface conditions, which is a marked improvement over conventional ISFET-style sensing where the device must be held in the saturation region via a fluid bulk potential.

2.2. Sensing gate preparation

To remove organic and surface contaminants, the CνMOS devices and witness samples were first cleaned by rinsing with acetone followed by methanol, isopropanol, and deionized water to avoid an undesired film from acetone. Next, the substrates were treated in a UV/ozone cleaning system (Bioforce Nanoscience) for 15 min. The substrate was then silanized by immersion in a mixture of 16.7% (v/v) (3-glycidoxypropyl)trimethoxysilane (3-GPS) (Acros Organics) in toluene (anhydrous 99.8%, Acros) for 1 h, followed by rinsing twice in toluene for 2 min at 45 rpm, drying with nitrogen, and baking at 120 °C for 1 hr to complete the hydrolysis reaction of the self-assembled monolayer (SAM). After baking, samples were stored in a nitrogen-purged dry box before protein application to avoid water reaching the surface.

Protein attachment was performed directly on silicon dioxide treated with 3-GPS. This attachment scheme provides substantial simplicity over (3-aminopropyl)triethoxysilane (APTS) and gold-thiol tethering techniques. Following preparation of the 3-GPS film, 0.2 mg/mL biotinylated bovine serum albumen (BSA) (Sigma) in 1× phosphate buffered saline (PBS) with pH 7.4 was applied to the sensors and witness samples for 2 h in a humidity chamber. After BSA was covalently bound to the 3-GPS, the devices were rinsed twice with 1× PBS for 2 min at 45 rpm to remove non-bound proteins, dipped in DI water to remove excess salt, dried with N_2, and then stored in 4 °C until use.

Before application of the target analyte, 40 μL of 0.1× PBS with pH 7.4 was applied to both sensor and witness samples by pipette. Sufficient time was allowed to stabilize the sensor readout. PBS applied at this step had 20% (v/v) glycerol added to reduce noise from convective fluid flow. Streptavidin was used as the target analyte (Pierce, Rockford, IL). 10 μL of streptavidin, in 0.02 mg/mL in 0.1× PBS, was added to sensor and witness samples. The measurement surroundings were made to closely resemble a humidity chamber to avoid fluid motion by surface evaporation.

Other protein capture systems were also characterized, including goat anti-mouse IgG (Pierce, Rockford, IL) as capture protein and mouse anti-rabbit IgG (Pierce, Rockford, IL) as target analyte with the BSA or tris blocking layer against non-specific binding. Film variation for this system was larger than the BSA/streptavidin system due to the smaller binding constant. For proof of concept, the more stable system was thus selected for the following presentation.

2.3. Ellipsometry thickness calibration

Film quality was assessed by measuring through ellipsometry the film thickness of each layer on witness silicon wafers at each step of the covalent attachment procedure. These measurements established the baseline properties of the films before and after measurements. An imaging ellipsometer (Nanofilm Surface Analysis) was employed with a 3-incident angle measurement at 69°, 70°, and 71° at a wavelength of 630.2 nm. A least-mean-square (LMS) fit for the data was used to estimate film thickness.

The surface concentration, Γ (ng/cm^2) and hence surface coverage of the organosilane and protein films are related to the refractive index and thickness (Cuypers et al., 1983) by

$$\Gamma \ (\mathrm{ng/cm^2}) = d\,\rho_o = d\frac{M_w}{A}\frac{n^2-1}{n^2+2} \quad (1)$$

Here, d is the thickness of the film, ρ_o the bulk density, M_w the molecular weight of the organosilane or protein (g/mol), A the molar refractivity of the material (cm^3/mol), and n is the index of refraction.

For protein, $M_w/A = 4.12$ g/cm^3 (Vogel et al., 1953) and the index of refraction was estimated from atoms or atom groups (Arwin, 1986) and found to be 1.542. For the organosilane, the index was taken as $n = 1.44$.

By estimating the molecular footprint or cross-sectional area, 0.25 nm^2 for the organosilane (Stevens, 1999) and 24.6 nm^2 for streptavidin calculated from 2.8 nm radius, the surface coverage (%) can be computed. For organosilane, ρ_o was assumed as 1.07 g/cm^3 and $M_w = 236.34$ g/mol. N_a is Avogadro's number:

$$\text{Surface coverage } (\%) = \frac{\Gamma N_a}{M_w} \times \text{molecular footprint} \quad (2)$$

2.4. Fluid delivery considerations

For fluid application during sensing, the sensor chip was placed in a plastic Petri dish and a 4-piece polydimethylsiloxane (PDMS) reservoir subsequently assembled on its surface to isolate sensing interface from electrical contact pads. Petri dish and PDMS pieces were cleaned with methanol, IPA, and DI water followed by N_2 dry (Fig. 1). The hydrophobic plastic surface effectively curbed wetting and served to eliminate leaks from the PDMS reservoir. The 4-piece reservoir proved robust and easy to assemble. It held up to 80 μL of fluid.

Low-frequency noise was present in the system and we attempted to reduce it by varying the PBS concentration and viscosity with the hypotheses that parasitic capacitive coupling and convective motion of contaminants may be culprits. 0.1× PBS appeared to give less noise than 1× PBS and was chosen for further testing. 0.01× and lower concentrations of PBS lost significant buffering capacity, which is necessary to make a stable, non-Faradaic electrochemical measurement (van Hal et al., 1996). Glycerol was introduced to reduce the effect of convection. With experimental verification, a 20% (v/v) mixture of glycerol to PBS gave the lowest noise and was chosen for subsequent tests. Though 20% (v/v) was used, viscosity is only increased by about 32% over pure water (Shankar and Kumar, 1994). Glycerol was not used for witness samples, since a small residue was found to interfere with ellipsometry measurements.

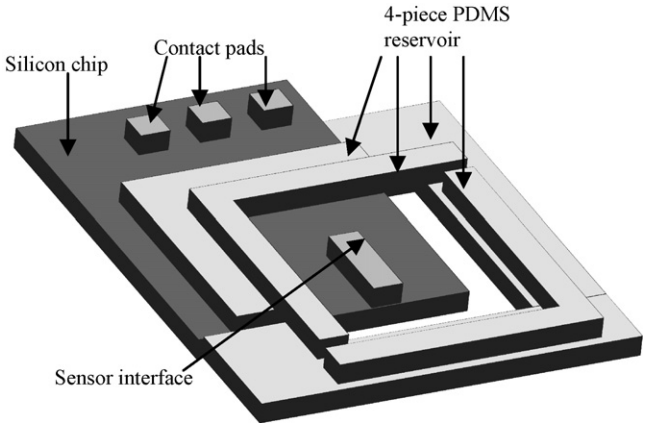

Fig. 1. Sensor chip with 4-piece PDMS reservoir assembled on surface. Chip and reservoir sit in hydrophobic Petri dish that limits leakage under chip and reservoir due to wetting.

2.5. Sensor models

The interaction of a functionalized SG surface with analyte in CνMOS can be approximated by an impedance model (Fig. 2a). The FG potential and the drain current will be affected as captured protein thickness grows, as seen in a small-signal model (Fig. 2b). Variables include dielectric constant (ε_r), capacitance of the native oxide layer (C_{oxide}), capacitance of the organosilane layer ($C_{3\text{-GPS}}$), capacitance of the BSA (C_{BSA}), and capacitance of the streptavidin layer (C_{strep}). To describe the fluid interface a Gouy–Chapman stern (GCS) model is used (Bard and Faulkner, 2004). C_{EDL} is the double layer capacitance, and C_{diff} is the diffusive capacitance of the GCS model. The small-signal device model consists of CG, drain (D), source (S), transconductance (g_m), output resistance (r_o), control gate capacitance (C_{cg}), sensing gate capacitance (C_{sg}) from interpoly-oxide, parasitic capacitance between floating gate and bulk (C_b), and floating gate potential relative to the source (v_{fgs}).

Many capacitive biosensor interface models include GCS components, though often they have minimal impact on calculation due to their large capacitance (Berggren et al., 2001). Descriptions of the interface/protein/fluid bulk system vary since the model best fitting the data with fewest parameters may not fully represent known physical phenomena (Berggren et al., 2001). Efforts have modeled protein deposition as a simple capacitor with varying thickness (Gebbert et al., 1992; Bergveld, 1991). Sensing across high-resistance oxide negates the need for a resistive component at the interface. Solution impedance is low and capacitance is high compared to other parts of the model so GCS layers can be dropped from the equivalent circuit without substantial loss of accuracy (Katz and Willner, 2003). By using a biological buffer fluid with a pH around the isoelectric point of the protein, the net protein charge is negligible, which makes sensor perturbation during capture depend only on impedance. For small-signal changes, modeling the protein membrane as strictly capacitance leads to reasonable results. For instance, an effort for real-time monitoring at 1 kHz for antigen–antibody binding across an oxide interface neglected resistive components of the protein membrane (Gebbert et al., 1992).

Equations for total FG capacitance (C_T), FG potential (V_{fg}), and large-signal saturation drain current (I_d) can be given as

$$C_T \cong C_b + C_{cg} + C_{sg}||C_{ox}||C_{3\text{-GPS}}||C_{BSA}||C_{strep} \\ ||C_{EDL}||C_{diff} \quad (3)$$

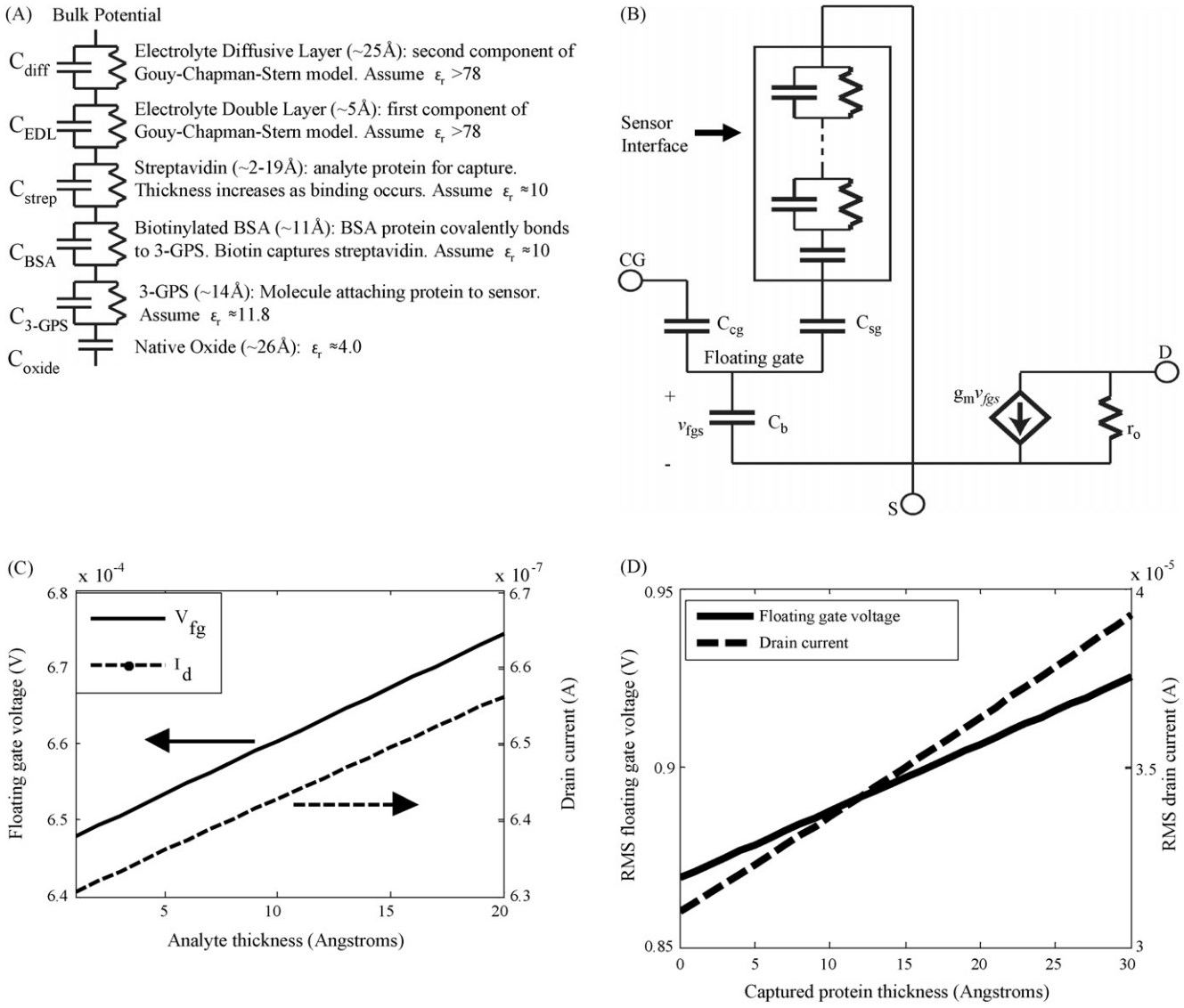

Fig. 2. (a) Impedance model of the sensor interface. (b) Small-signal model for CνMOS device in saturation. Source is tied to bulk. (c) Simulated small-signal response against protein thickness variation with 5 V large-signal bias on both CG and drain, and 0.1 V small signal on CG. Model assumes typical values for sensor capacitance listed in (a). (d) Simulated large-signal response in the saturation region against protein thickness variation with 10 V peak-to-peak sinusoidal waveform with zero DC offset.

$$V_{\mathrm{fg}} \cong \frac{Q + V_{\mathrm{cg}}\, C_{\mathrm{cg}}}{C_{\mathrm{T}}} \tag{4}$$

$$I_{\mathrm{d}} = \frac{\kappa_{\mathrm{n}}}{2}(V_{\mathrm{fg}} - V_{\mathrm{t}})^2 \tag{5}$$

Here, Q is the static charge on the floating gate, κ_{n} the transconductance parameter, and V_{t} is the threshold voltage.

The FET operation points can also be set by a large-signal sinusoidal bias on CG whose period is much shorter than the expected protein growth time. From a large-signal model, the drain current is a quadratic function of the FG potential when the DC bias is set in the above-threshold saturation operation. Computed responses from both the small-signal model (Fig. 2c) and large-signal model (Fig. 2d) can be seen, with Fig. 2d appearing linear due to the small range of protein thickness presented.

The bulk potential is assumed to be zero, since it connects to ground through fringing fields. As analyte capture occurs, effective thickness and area coverage percentage of the streptavidin layer increase, affecting total floating gate potential by the change in capacitance of the protein layer through C_{T} in Eq. (4). Notice that the capture may not happen homogeneously on the sensing surface. By proper geometrical design in CνMOS, the capacitance viewing from SG dominates the capacitive network to maximize sensitivity of the analyte activity.

2.6. Measurement setup and large-signal data extraction

A 10 Vpp AC voltage from a function generator (Stanford Research DS345) was provided to CG input and to the reference input of a lock-in amplifier (Stanford Research 830) with Drain and Source terminals biased at 5 and 0 V, respectively (Fig. 3).

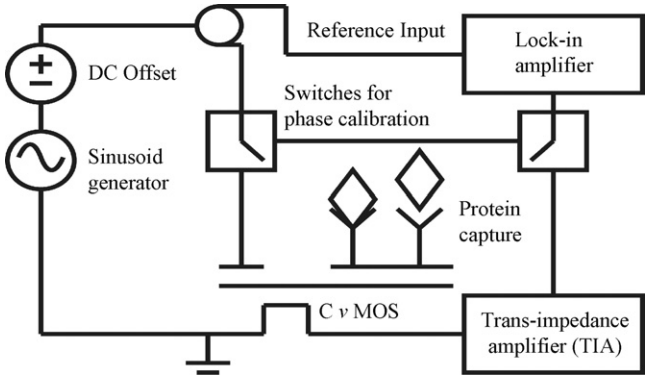

Fig. 3. CνMOS sensor in measurement circuit. AC signal is delivered to control gate, creating an alternating field that both probes the sensor interface and creates inversion in FET. Drain current is converted to voltage by the TIA and monitored by the lock-in amplifier.

The AC signal both probes the sensing interface and creates inversion in the FET when the FG potential exceeds the threshold voltage. Phase calibration for a given measurement results from using the switches and allows measurements to calibrate phase at each frequency point, thus preserving phase data to enhance information extraction. The output drain current is transduced to a voltage and fed to both the lock-in amplifier at 100 μA/V (Stanford Research SR570) and oscilloscope (Tektronix TDS 340 A) for analysis. In this paper, we analyze the data from the lock-in amplifier, using oscilloscope images to monitor total waveform integrity. The CG sinusoid creates an AC field on FG and in turn on SG. The SG field probes the protein layers and the surrounding fluid up to the Debye length, which is about 25 Å by the PBS concentration.

The CνMOS and sensor interface models were calibrated against pre-capture conditions and then the effective analyte thickness was extracted after the capture event. For the sensor interface model, ellipsometer-measured thickness on witness samples was used to estimate the capacitance by a parallel plate model:

$$C = \frac{\varepsilon_o \varepsilon_r A}{d} \tag{6}$$

Here, ε_o is the vacuum permittivity and A is the surface area (cm^2). ε_r was assumed as 4.5, 11.8, 10, and >78 for SiO_2, 3-GPS, protein, and water, respectively. The precise values of ε_r for the layers do not matter much since the model is calibrated prior to thickness extraction. As mentioned, the GCS capacitive layers have large values and are dropped without substantial loss of accuracy. With these capacitances as well as C_b and C_{cg}, all capacitances can be known. With κ_n and V_t obtained from the foundry technology file, the large-signal equation for I_d in Eq. (5) can be expressed as a variable of V_{fg} in Eq. (4) which depends on Q. For model calibration, The RMS value of I_d was matched between the CνMOS model and measured pre-capture conditions by adjusting Q. After calibration, Q was held constant and V_{fg} was allowed to affect I_d by varying captured protein thickness d in Eqs. (3) and (6). After protein capture, a final protein thickness was determined such that the CνMOS model matched the measured RMS value of drain current.

Sensing shown in this paper involves measurements over time at a single frequency (20 kHz). The simple capacitor divider does not have frequency dependence. As will be shown, the assumption of a purely capacitive layer worked well for small variations of protein thickness.

2.7. Sensor re-use

In order to re-use sensors after protein detection, a 2-stage plasma etch was applied. In a reactive-ion-etch (RIE) tool, the chips were first exposed to a 30 sccm O_2, 60 mTorr, 150 W etch for 1 min to remove all top organic matter, followed by a 50 sccm CHF_3, 5 sccm O_2, 40 mTorr, 200 W etch to remove the Si portion of 3-GPS, SiO_2, and organic matter. This combination of etches resulted in a slightly thicker native oxide (~30 Å) than is found on fresh wafers exposed to HF dip (~20 Å).

3. Results

Fig. 4 shows real-time RMS response to a protein capture events and control test measured at 20 kHz. The capture event corresponds to analyte thickness change of 18.6 Å or roughly 69% surface coverage and 3.0 Å or roughly 11% surface coverage. The capture event shows a clear rise in signal after the analyte is added. The signal saturates as available surface sites become occupied. The control test shows no net change after a same-size drop of PBS is added.

An interface device cannot sample the entire bulk solution and instead only captures a small fraction of the solution bulk, depending on the bulk concentration and available binding sites on the surface. The result can be used to infer protein concentration. Irreversible binding of streptavidin and biotin allows for very accurate ellipsometric measurements to create an accurate

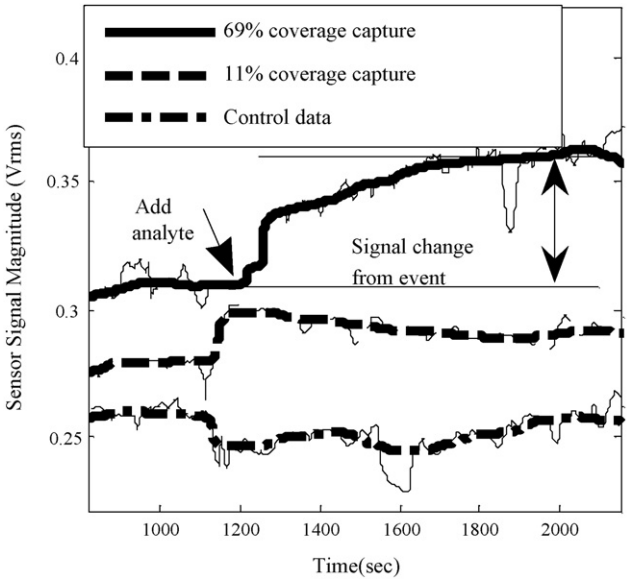

Fig. 4. Real-time detection of roughly 18.6 Å (or roughly 69% surface coverage) and 3.0 Å (roughly 11% surface coverage) of streptavidin binding to biotinylated BSA and control test in electrolytic fluid at 20 kHz CG signals. Median-filtered and real-time data are presented.

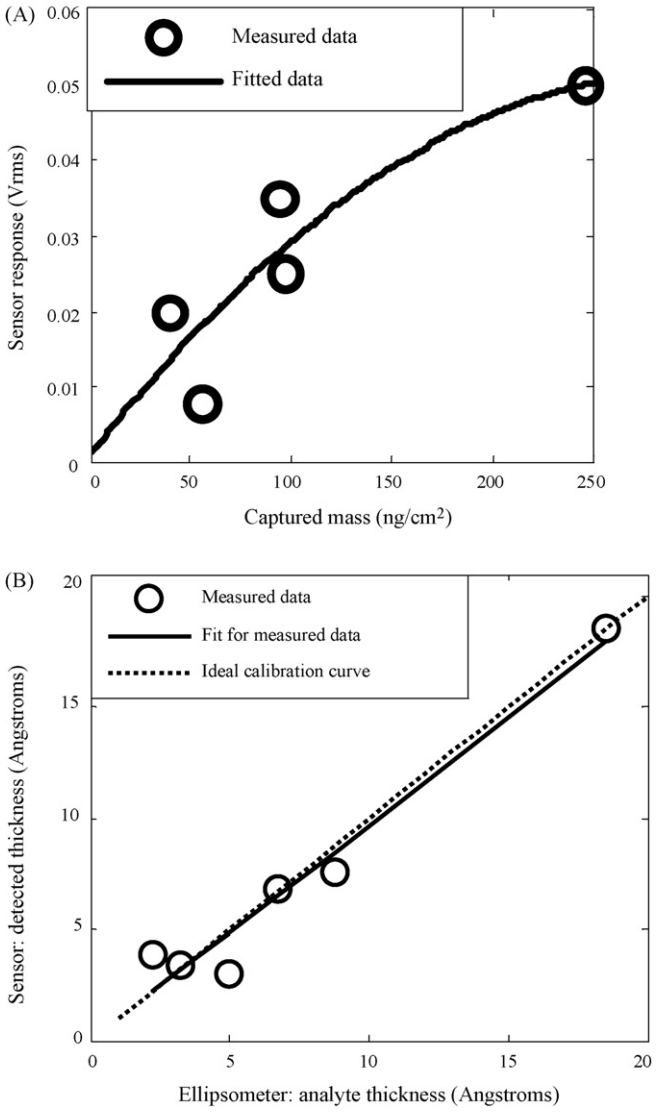

Fig. 5. Calibration curves constructed from 20 kHz sensor monitoring over several samples. (a) Sensor response versus protein mass absorbed on sensor surface calculated from thickness measured by ellipsometer. Data is fitted with quadratic function to account for large-signal contribution to sensor response. (b) Detected thickness extracted from large-signal sensor model versus analyte thickness measured by ellipsometer on witness samples. Protein thickness measured by ellipsometer can be converted to surface coverage, here ranging from 11% to 69%. The fit for measured data yields a slope of 0.99 and an intercept of 0.16 Å.

calibration curve for mass bound to the surface. Several sensor responses to protein binding as measured against control samples can be used to construct the calibration curves in Fig. 5. Results are shown after available binding sites have been saturated and contain no time information. Fig. 5a shows raw and fitted data with sensor response plotted against mass of absorbed protein on sensor surface calculated with ellipsometer-measured thickness. A quadratic fit was used to account for the effect capacitance change has on the large-signal drain current equation. Streptavidin thickness was measured to vary between 3.0 and 18.6 Å. Fig. 5b shows the results of extracted thickness from sensor models in Fig. 2 against that from ellipsometer on the witness samples. Using Eq. (2), surface coverage for captured analyte can be estimated to range from 11% to 69%. Care was taken to ensure the sensor and witness samples experienced the same treatment throughout the experiment aside from a difference in glycerol in the analyte solution. A fit between actual and extrapolated thickness values gives a slope of 0.99 and a y-intercept of 0.16 Å.

4. Discussions

4.1. Detection sensitivity and model accuracy

Fig. 5a shows resolution of approximately 25 ng/cm^2 or 2 Å change in streptavidin layer corresponding to a 13.7 mV sensor response with a dynamic resolution on the order of 50 s. In principle, with improved noise floor the sensor can detect 1 ng/cm^2 deposition for roughly a 500 μV sensor response based on calibration curve findings. Sensor response begins to saturate near 250 ng/cm^2, which corresponds to roughly 18.6 Å and 69% surface coverage. Good sensitivity is observed between 11% and 69% surface coverage. For 20 kHz and up to 20 Å of captured protein, modeling the sensor interface as capacitance only without resistance gives substantial accuracy. Both unprocessed sensor data versus captured mass (Fig. 5a) and data processed with large-signal extraction model (Fig. 5b) can be used for calibration. Agreement with the small-signal model (Fig. 2c) is also observed as sensor signal increases with analyte thickness or captured mass.

The saturation of raw data indicates the saturation of available surface sites. Detection shows the results of captured mass, or amount of streptavidin bound to biotin at the surface. With an insignificant reverse reaction constant, any molecule that reaches an unoccupied site on the surface will likely remain bounded.

4.2. Net ion drift

Low-frequency signal drift is a persistent problem in FET-based sensors. The AC measurement scheme reduces problematic low-frequency signal drift for a dry chip previously exposed to PBS (Fig. 6a) by eliminating net ion drift in oxide. Drift is assumed to come from Na^+ ions, which are highly mobile in silicon dioxide (Razavi, 2001). Negligible drift is seen for a sinusoid applied to the control gate with no DC offset while the same conditions with small DC offset causes net drift in the signal. With drift reduced, noise reduces to random variations. This can dramatically reduce the complexity in stabilization circuitry or signal post-processing. Though AC measurement can reduce drift, future device design may also include silicon nitride passivation layers to reduce ion contamination.

4.3. Noise analysis

Electrochemical and biological events can add significant noise to a sensor signal. Noise at interface often assumes a $1/f^{\alpha}$ form with α varying from 0 to 2. Many chemical and biological processes exhibit $1/f$ noise behavior, similar to semiconductor devices where $1/f$ noise results from interface trapping and detrapping such as from dangling bonds, substrate noise

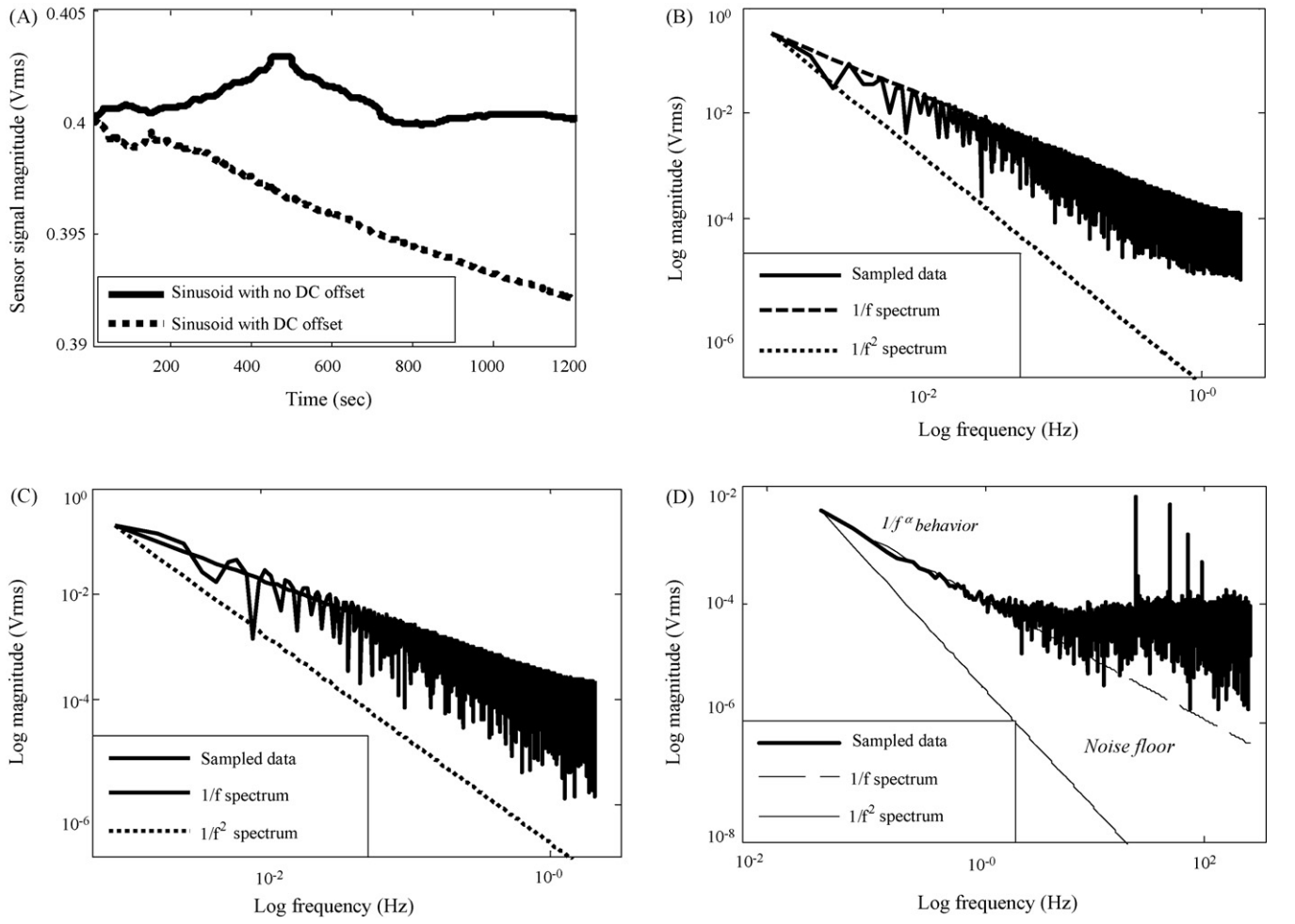

Fig. 6. (a) Comparison of low-frequency drift with and without 0.5 V DC offset without applying fluid on the sensing interface. (b) Noise spectrum of the capture event. $1/f^{\alpha}$ profile conforms to $\alpha = 1.2$. (c) Noise spectrum immediately after capture. Noise profile conforms to $\alpha = 1.0$, as expected from background electrolyte fluctuations. (d) Noise spectrum of a control test with PBS on sensor interface at increased sampling rate shows frequency-independent noise floor starting around 1 Hz. Noise profile at low frequencies conforms to $1/f$, as expected from background electrolyte.

effects, mobility fluctuations, and carrier concentration fluctuations (Buckingham, 1983; Razavi, 2001; Vandamme et al., 1994; Dutta and Horn, 1981). $1/f$ noise in a biological context (Siwy and Fulinski, 2002) can result from ion-channel noises and concentration fluctuation (White et al., 2000; Bezrukov, 2000), protein trapping and detrapping, or conformational changes. Stochastic models of protein binding have predicted $1/f^2$ variation from a single binding event (Hassibi et al., 2004, 2005).

A Fourier transform of a capture event and control test demonstrates low-frequency noise with dependence between $1/f$ and $1/f^2$ (Fig. 6b–d). If noise takes the form $1/f^{\alpha}$, $\alpha = 1.20$ for the full-capture event, as expected for a step function (Fig. 6b). Sensor response after capture shows low-frequency behavior with $\alpha = 1.00$ (Fig. 6c). Pre-capture response is equivalent to a control test (Fig. 6d). Curiously, the noise starts to reach a frequency-independent noise floor around 1 Hz. The sampling rate was increased for a control test to 512 Hz on the 20 kHz CG signal. This extends the noise plot out to 256 Hz, and shows the noise floor in addition to low frequency $1/f$ behavior (Fig. 6d). For smaller sensors, comparing differences in noise profiles of a captured protein and control tests may yield resolution of binding interactions of a single protein molecule. For example, this may be seen by Fig. 6c showing greater noise than Fig. 6d below 1 Hz, indicating trapping and detrapping protein–protein events.

We see the frequency dependence of noise decreasing at higher frequencies, indicating the presence of either white noise or shot noise, both of which are almost frequency independent. Shot noise, the noise associated with carrier injection across a barrier, in contrast to $1/f$ noise, is purely random with no frequency dependence of the noise power density. It is readily observed with carrier injection across a p–n junction in semiconductor devices, but also has a predicted counterpart in miniaturized, affinity-based biosensors (Hassibi et al., 2005). Shot noise in biological systems is hardly documented, in part because it is difficult to distinguish it from white noise. Determination of the dominant noise source can be found by varying the probing amplitude. If the noise level shows strong dependence on signal magnitude at higher frequencies, then shot noise dominates

Implications from $1/f^{\alpha}$ and shot noise for sensors and sensor circuits include the need to observe for relatively long time scales in order to account for substantial low-frequency varia-

tion. Low-noise circuits are required so that $1/f$ noise from the circuit can be distinguished from that of the fluid. Spectroscopic measurements need to be sampled and filtered to reduce detrimental effects from fluctuations. It will be beneficial to include dummy sensors for differential signal generation. If indeed ion fluctuation is the cause of $1/f$ noise, convection flow or agitator should be added so that the fluid stays mixed.

4.4. False negatives and diffusion time

Adequate time is needed for added analyte to reach the sensor surface by diffusion and convection. At the concentrations used, streptavidin requires between 40 min and 90 min to diffuse across a 50 μL PBS sphere and reach 50% surface coverage on the sensor surface by the 1D diffusion model of Eq. (7) (Anner, 1990):

$$N(x,t) = N_o \,\mathrm{erfc}\left(\frac{x}{\sqrt{4Dt}}\right) \tag{7}$$

Here, $N(x, t)$ is the concentration (M), N_o the concentration at the source, erfc the complementary error function, and D (cm^2/s) is the diffusion constant. A diffusion constant of 7.4×10^{-7} cm^2/s for streptavidin (Raschke et al., 2003) is used for estimation. Diffusion time is the required time to bring occupied surface sites to 50% surface coverage, which is modeled by the Langmuir model for occupied surface sites:

$$\theta = \frac{\alpha\, N(x,t)}{1 + \alpha\, N(x,t)} \tag{8}$$

Here, θ is the fraction of occupied surface sites and α is the binding constant between proteins. The biotin/streptavidin system has one of the largest free energies of association for non-covalent binding of a protein and small ligand and is often used in tethering schemes with proteins such as BSA. For biotin and streptavidin, $\alpha = 10^{14}\ M^{-1}$ in free solution, but will be reduced due to the binding of biotin to BSA and tethering to the sensor surface, which restricts motion Reduced α will result in more time needed for binding to occur.

Successful tests gave an increase in sensor response much earlier than 40 min, indicating convection decreased transport time over diffusion alone. The likely source was pipette injection. A diffusion-limited test may mistakenly be recorded as a false negative if stopped too early. In order to avoid false negatives the distance traveled by the analyte should be decreased or convection should be added to the system.

5. Conclusions

CνMOS was shown to detect streptavidin binding to BSA by monitoring at a single AC frequency. The platform was fabricated entirely through silicon foundry process with post-processing involving application of SAM for protein capture. Gold and platinum were not used. A model of the sensor and sensor interface was established and gave good agreement with experiments. CνMOS is shown to resolve streptavidin changes on the order of 25 ng/cm^2 or 2 Å as verified against ellipsometry on witness samples, with possible 2 ng/(cm^2 mV) detection limit. The measurement scheme helps to reduce signal drift. $1/f^{\alpha}$ and frequency independent noise floor of fluid was discussed.

Acknowledgements

This work is supported by EPA, Sandia National Laboratories, and NYSTAR.

References

Anner, G.E., 1990. Planar Processing Primer. Van Nostrand Reinhold Company, NY.
Arwin, H., 1986. Appl. Spectrosc. 40 (3), 313–318.
Bakker, E., 2004. Anal. Chem. 76 (12), 3285–3298.
Barbaro, M., Bonfiglio, A., Raffo, L., 2006. IEEE Trans. Electron Dev. 53 (1), 158–166.
Bard, A.J., Faulkner, L.R., 2004. Electrochemical Methods. Wiley, Hoboken, NJ.
Berggren, C., Bjarnason, B., Johansson, G., 2001. Electroanalysis 13 (3), 173–180.
Bergveld, P., 1991. Biosensors Bioelectron. 6 (1), 55–72.
Bergveld, P., 2003. Sensors Actuat. B: Chem. 88 (1), 1–20.
Bezrukov, S.M., 2000. J. Membr. Biol. 174 (1), 1–13.
Buckingham, M.J., 1983. Noise in Electronic Devices and Systems. Ellis Horwood Limited, West Sussex, England.
Cane, C., Gotz, A., Merlos, A., Gracia, I., Errachid, A., Losantos, P., Lora-Tamayo, E., 1996. Sensors Actuat. B: Chem. 35 (1), 136–140.
Cuypers, P.A., Corsel, J.W., Janssen, M.P., Kop, J.M.M., Hermens, W.T., Hemker, H.C., 1983. J. Biol. Chem. 258 (4), 2426–2431.
DeSilva, M.S., Zhang, Y., Hesketh, P.J., Maclay, G.J., Gendel, S.M., Stetter, J.R., 1995. Biosensors Bioelectron. 10 (8), 675–682.
Drummond, T.G., Hill, M.G., Barton, J.K., 2003. Nat. Biotechnol. 21 (10), 1192–1199.
Dutta, P., Horn, P.M., 1981. Rev. Mod. Phys. 53 (3), 497–516.
Gebbert, A., Alvarez-Icaza, M., Stocklein, W., Schmid, R.D., 1992. Anal. Chem. 64 (9), 997–1003.
Hassibi, A., Navid, R., Dutton, R.W., Lee, T.H., 2004. J. Appl. Phys. 96 (2), 1074–1082.
Hassibi, A., Zahedi, S., Navid, R., Dutton, R.W., Lee, T.H., 2005. J. Appl. Phys. 97, 084701.
Hassibi, A., Lee, T.H., 2006. IEEE Sensors J. 6 (6), 1380–1388.
Jacquot, B.C., Muñoz, N.L., Kan, E.C., 2006. Proceedings of the 28th International Conference. IEEE Engineering in Medicine and Biology Society, New York, NY, pp. 1846–1849.
Jacquot, B.C., Lee, C., Shen, Y.N., Kan, E.C., 2005. Proceeding of IEEE Sensors, Anneheim, CA, pp. 101–104.
Katz, E., Willner, I., 2003. Electroanalysis 15 (11), 913–947.
Minch, B.A., Diorio, C., Hasler, P., Mead, C.A., 1996. Analog Integr. Circ. Signal Process. 9 (2), 167–179.
http://www.mosis.org/Technical/Processes/proc-ami-abn.html.
Pei, R., Cheng, Z., Wang, E., Yang, X., 2001. Biosensors Bioelectron. 16 (6), 355–361.
Radke, S., Alocilja, E., 2004. IEEE Sensors J. 4 (4), 434–440.
Raschke, G., Kowarik, S., Franzl, T., Sonnichsen, C., Klar, T.A., Feldmann, J., Nichtl, A., Kurzinger, K., 2003. Nano Lett. 3 (7), 935–938.
Razavi, B., 2001. Design of Analog CMOS Integrated Circuits. Tata McGraw-Hill, New York, NY.
Sadik, O.A., Xu, H., Gheorghiu, E., Andreescu, D., Balut, C., Gheorghiu, M., Bratu, D., 2002. Anal. Chem. 74 (13), 3142–3150.
Saum, A.G.E., Cumming, R.H., Rowell, F.J., 1998. Biosensors Bioelectron. 13 (5), 511–518.
Shankar, P.N., Kumar, M., 1994. Proc. Math. Phys. Sci. 444 (1922), 573–581.
Shen, N.Y., Liu, Z., Lee, C., Minch, B.A., Kan, E.C., 2003. IEEE Trans. Electron Dev. 50 (10), 2171–2178.

Shen, N.Y., Liu, Z., Jacquot, B.C., Minch, B.A., Kan, E.C., 2004. Sensors Actuat. B: Chem. 102 (1), 35–43.
Shibata, T., Ohmi, T., 1992. IEEE Trans. Electron Dev. 39 (6), 1444–1455.
Siwy, Z., Fulinski, A., 2002. Phys. Rev. Lett. 89 (1), 158101.
Stevens, M.J., 1999. Langmuir 15 (8), 2772–2778.
Thevenot, D.R., Toth, K., Durst, R.A., Wilson, G.S., 2001. Anal. Lett. 34 (5), 635–659.
Vandamme, L.K.J., Li, X., Rigaud, D., 1994. IEEE Trans. Electron Dev. 41 (1), 1936–1945.
van Hal, R.E.G., Eijkel, J.C.T., Bergveld, P., 1996. Adv. Colloid Interf. Sci. 69 (1), 31–62.
Vogel, A.I., Cresswell, W.T., Leicester, J., 1953. J. Phys. Chem. 58 (2), 174–177.
White, J.A., Rubinstein, J.T., Kay, A.R., 2000. Trends Neurosci. 23 (3), 131–137.
Wilson, D.M., Hoyt, S., Janata, J., Booksh, K., Obando, L., 2001. IEEE Sensors J. 1 (4), 256–274.